Journal of The Electrochemical
Society

Combinatorial Study of the Si-Sn-O System as Negative Electrode Materials in Li-Ion Cells

To cite this article: Xiuyun Zhao *et al* 2016 *J. Electrochem. Soc.* **163** A203

Journal of The Electrochemical Society, **163** (2) A203-A209 (2016)

Combinatorial Study of the Si-Sn-O System as Negative Electrode Materials in Li-Ion Cells

Xiuyun Zhao,[a,b,c,*] M. T. Schreiber,[a,b,c] L. MacEachern,[a,b,c] R. J. Sanderson,[a,b] R. A. Dunlap,[a,b,d] and M. N. Obrovac[a,b,c,,z]**

[a] *Department of Physics and Atmospheric Science, Dalhousie University, Halifax, Nova Scotia B3H 4R2, Canada*
[b] *Institute for Research in Materials, Dalhousie University, Halifax, Nova Scotia B3H 4R2, Canada*
[c] *Department of Chemistry, Dalhousie University, Halifax, Nova Scotia B3H 4R2, Canada*
[d] *College of Sustainability, Dalhousie University, Halifax, Nova Scotia B3H 4R2, Canada*

$Si_xSn_yO_{1-x-y}$ films with $0.45 < x < 0.80$, $0.05 < y < 0.35$, and $0.05 < (1-x-y) < 0.40$ have been prepared using a magnetron sputtering method. All compositions had an amorphous structure and good capacity retention. Reversible volumetric capacities exceeding 2000 Ah/L were obtained in films with high Si or Sn content. The initial coulombic efficiency becomes reduced when the oxygen content is increased, as increasing the oxygen content in these films causes a reduction in reversible capacity. Surprisingly, however, the oxygen content does not substantially increase the irreversible capacity. Further work should focus on improving the initial coulombic efficiency of Si-Sn-O electrodes.

Manuscript submitted September 2, 2015; revised manuscript received October 19, 2015. Published November 17, 2015.

The demand for high-performance lithium-ion batteries is increasing due to their widespread use in consumer electronics and electric vehicles. Si-based and Sn-based alloys are of considerable interest as negative electrode materials because they have the potential to deliver higher volumetric energy density when compared to traditional graphite electrodes.[1] However, crystalline alloys can suffer from inhomogeneous volume changes if 2-phase regions are encountered during lithiation. This can cause particle pulverization, poor electrical contact, and capacity loss.[2–4] By comparison, amorphous and nanocrystalline alloys have been found to show improved cycling performance due to their reversibly homogeneous volume change.[4–7] Capacity loss may also occur in amorphous alloys when electrical contact is lost due to mechanical failure of the electrode coating as the alloy particles expand and contract during cycling.[4] One possibility to reduce contact loss is by surrounding active materials with an inactive matrix that can dilute the volume changes.[2,8] As well, it has been shown that alloying inactive elements with active elements actually results in increased volumetric energy density at a given volume expansion.[8] Thus, amorphous active/inactive alloys are promising as negative electrode materials for Li-ion batteries.

One of methods to rapidly explore the chemistry of amorphous active/inactive alloys based on Si and Sn is by sputter deposition. The sputtering system developed by Dahn et al. makes it possible to obtain composition-spread films and investigate the range of amorphous phase formation, as well as the relation between composition, structure and electrochemical performance.[9] Many researchers have investigated the electrochemical performance of sputtered deposited amorphous or nanostructured Si-Sn films in lithium batteries.[4–7,10–13] Hatchard et al. found that $Si_{1-x}Sn_x$ ($0 < x < 0.5$) alloy films with $x < 0.5$ are amorphous and show excellent cycling performance.[7,12] They also showed that the initial coulombic efficiencies (ICE) of these films can be very high (ICE = 95% when $x = 0.45$). Al-Maghrabi et al. studied Si-Sn-C thin films and showed that the addition of carbon to Sn-Si inhibits the aggregation of Sn into regions of relatively pure tin.[14] Dahn et al. have found that introducing rare earths to $Si_{1-x}Sn_x$ films can reduce the reversible capacity of amorphous Si-Sn alloys without negative impact on capacity retention.[15] These previous results make Si-Sn based alloys of considerable interest as electrodes for Li-ion batteries.

The effect of oxygen in thin films is important to consider, since considerable oxygen content can be included in alloys during their synthesis. In materials like SiO_x the presence of oxygen is believed to reduce the ICE substantially, due to the irreversible reaction of Li to form lithium silicates during the first discharge/charge cycle. However, once formed, the lithium silicates are thought to act as a lithium ion conducting inactive phase which both reduces overall volume expansion and improves rate capability.[16,17] Al-Maghrabi et al. prepared $Si_{1-x}O_x$ ($0.1 < x < 0.4$) films using combinatorial sputtering methods. They found that increasing the oxygen content leads to an increase in irreversible capacity, but that the creation of the Li_4SiO_4 inactive phase may help improve cycling. On the other hand, they observed that increasing oxygen content introduces extra high voltage capacity.[18] Nguyen et al. made SiO_x films ($x = 0.4$, 0.85, 1.0 and 1.3) by pulsed laser deposition and investigated the effects of oxygen content on cycling performance. They found higher oxygen content of SiO_x decreases initial electrolyte reduction, whereas a larger fraction of oxides is subjected to dissolution by acid (e.g., HF)-etching in a 1 M $LiPF_6$/ethylene carbonate / diethyl carbonate electrolyte. This might be the reason why the capacity fluctuates during cycling for the electrodes with higher oxygen content.[19]

For SnO_x electrode materials, the oxygen can bond irreversibly with lithium to form an amorphous Li_2O matrix during the first discharge process. This lithia "matrix" helps to keep the electrode particles mechanically connected and improves cycling, however this can lead to irreversible initial capacity loss.[20,21] The electrochemistry of SnO and SnO_2 thin films prepared by various methods in lithium batteries has been reviewed recently by Reddy et al.[22] Such films have high irreversible capacities due to the irreversible formation of Li_2O. This can result in cells with low energy density.[1]

Considering the good cycling performance of Sn oxides, the introduction of conductive Sn to SiO_x may improve electrochemical performance. Little research, however, has been reported on the electrochemistry of the Si-Sn-O system. Courtney et al. have studied $SiSnO_3$ glass as an electrode of lithium cells and carried out in-situ XRD experiments. They found Li_2O formed as well as SiO_2 during the first discharge process. They also proposed that the resulting SiO_2 prevented the formation of bulk Li-Sn phases, and thus improved cycling.[20] The goal of the present work is to make a systematic study of the Si-Sn-O system using combinatorial methods and to explore the role of oxygen on its electrochemical performance.

*Electrochemical Society Student Member.
**Electrochemical Society Active Member.
[z] E-mail: mnobrovac@dal.ca

Experimental

$Si_xSn_yO_{1-x-y}$ samples were produced by magnetron sputtering. The sputtering system used was a modified Corona V3-T magnetron deposition system (Corona Vacuum Coaters, Vancouver, BC Canada), as described by Dahn et al.[9] Si, SiO_2, and Sn sputtering targets (50 mm diameter by 6 mm thickness, 99.999% pure) were obtained from Kurt J. Lesker. Three different masks used for the targets: a constant mask for the Si target, a linear-in mask for the SiO_2 target, and a linear-out mask for the Sn target. The sputtering powers used were 100 W DC for Si, 140 W RF for SiO_2, and 15 W DC for Sn. The deposition was done under an argon gas pressure of 1.0 ± 0.2 mTorr. The substrate table angular speed was approximately 15 rpm. $Si_xSn_yO_{1-x-y}$ films were deposited on one 76.2×76.2 mm Si (100) wafer (used for X-ray diffraction studies), one 76.2×76.2 mm glass plate covered with Cu (used for composition determination), and an array of 25 preweighed 12.6 mm diameter Cu foil disks (used to determine the mass per unit area of the film over the deposition area and for electrochemistry studies).

XRD measurements were performed using an INEL CPS120 curved position-sensitive detector coupled to an X-ray generator equipped with a Cu target X-ray tube. A JEOL JXA-8200 Superprobe coupled to a programmable x-y translation stage was used to determine the composition as a function of position on the films. A Sartorius SE-2 microbalance (0.1 μg precision) was used to measure the mass of the Cu disks before and after sputtering. A Phenom G2-pro Scanning Electron Microscope (SEM, Nanoscience, AZ) was used to observe the thickness of the sputtered films.

The electrochemical performance of the $Si_xSn_yO_{1-x-y}$ films was characterized using 2325 coin cells. The electrolyte was a 1 M $LiPF_6$ ethylene carbonate / diethyl carbonate / monofluoroethylene carbonate (30/60/10 v/v/v) solution. Cells were assembled with a $Si_xSn_yO_{1-x-y}$ working electrode, two Celgard 2300 separators, and a lithium foil counter/reference electrode in an argon-filled glove box. Cells were cycled with a Maccor Series 4000 Automated Test System at a C/10 rate and trickled discharged to C/20 in the voltage range of 0.005–0.9 V. The theoretical capacity of the $Si_xSn_yO_{1-x-y}$ films was calculated assuming the Si and Sn react with Li to form $Li_{15}Si_4$ and $Li_{22}Sn_4$, respectively, while O does not react with lithium.

Results and Discussion

Compositions as obtained from microprobe analysis were confirmed by "library closure"[23] as shown in Figure 1. In this figure the composition and mass per unit area of a typical library as a function of position along the library is plotted. Figure 1a shows moles per unit area of Si, O, and Sn as defined by the "constant and linear in", "linear-in" and "linear-out" sputtering masks, respectively. Figure 1b compares the measured mass of the sputtered films on each weigh disk (squares) with the calculated mass (solid line) from the curves in Figure 1a for a $Si_xSn_yO_{1-x-y}$ library. This comparison shows that the measured compositions are consistent with the expected compositions based on mask geometry. Figure 1c shows that the mole fractions of Si, Sn and O (solid line) calculated from Figure 1a agree with the compositions measured by wavelength dispersive spectroscopy (WDS). Therefore the sputtered compositions as determined by WDS are near the expected compositions from the mask geometry and are moreover consistent with the measured film mass.

The composition range of the sputtered Si-Sn-O film is shown in a ternary diagram in Figure 2. Each point in the diagram represents the composition of one of the 25 electrodes tested coin cells. XRD measurements were also made at these compositions. In order to better understand the effects of each element in the ternary system on the structure and electrochemistry of the sputtered Si-Sn-O, the samples at the points along the three lines L1, L2 and L3, corresponding to $x \approx 0.50$, $y \approx 0.10$, and $(1\text{-}x\text{-}y) \approx 0.10$, respectively, were selected for detailed analysis. A comparison is also made between the samples at the most Si, Sn and O-rich compositions prepared (P1, P2 and P3, respectively).

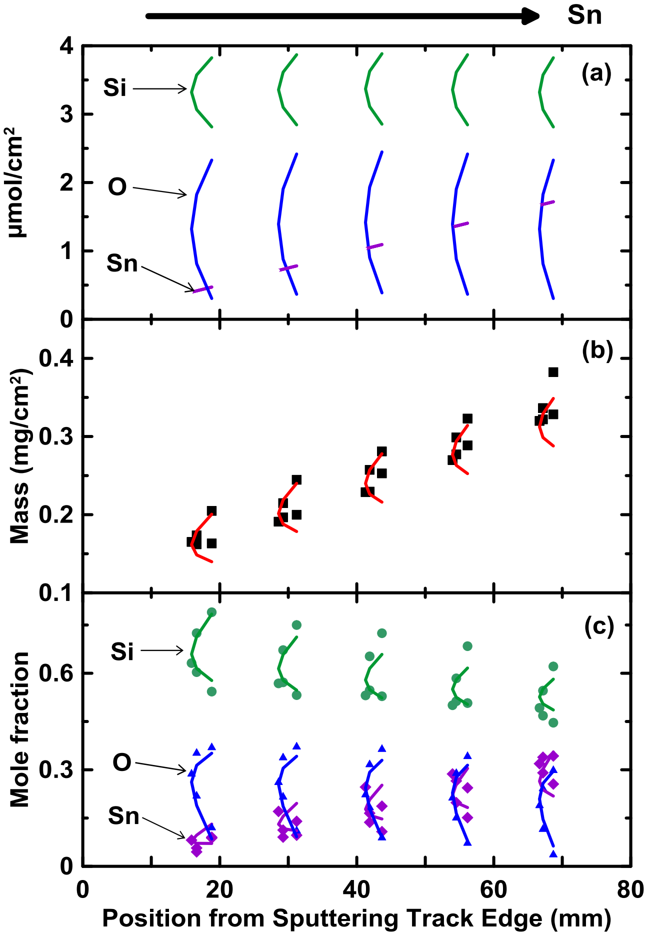

Figure 1. Plots illustrating closure of the $Si_xSn_yO_{1-x-y}$ sputtered library. (a) The moles per unit area of Si, Sn, and O defined by "constant and linear in", "linear out" and "linear in" sputtering masks, respectively. (b) Calculated mass per unit area based on (a) agrees with the measured mass. (c) The compositions calculated from (a) shows agreement with the measured values from wavelength dispersive spectroscopy. Solid lines: Calculated; Symbols: Experimental.

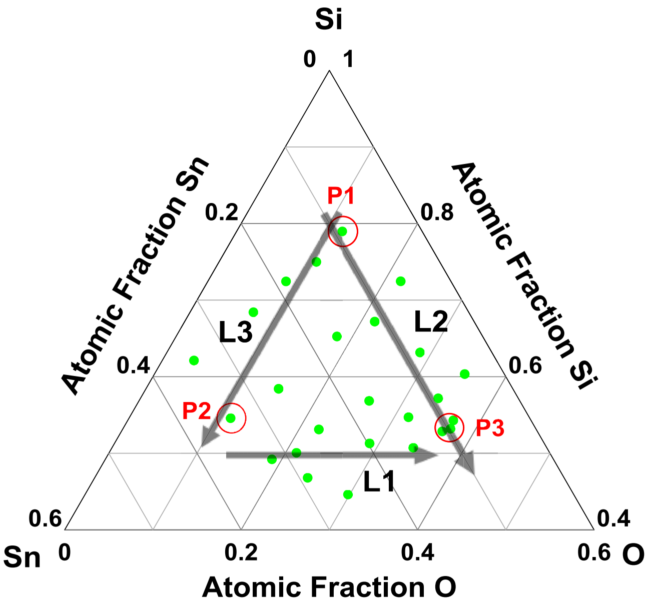

Figure 2. Gibbs triangle showing compositions as determined by electron microprobe analysis. Line 1: x = 0.5; line 2: y = 0.1; and line 3: (1-x-y) = 0.1. P1: Si rich; P2: Sn rich; and P3: O rich.

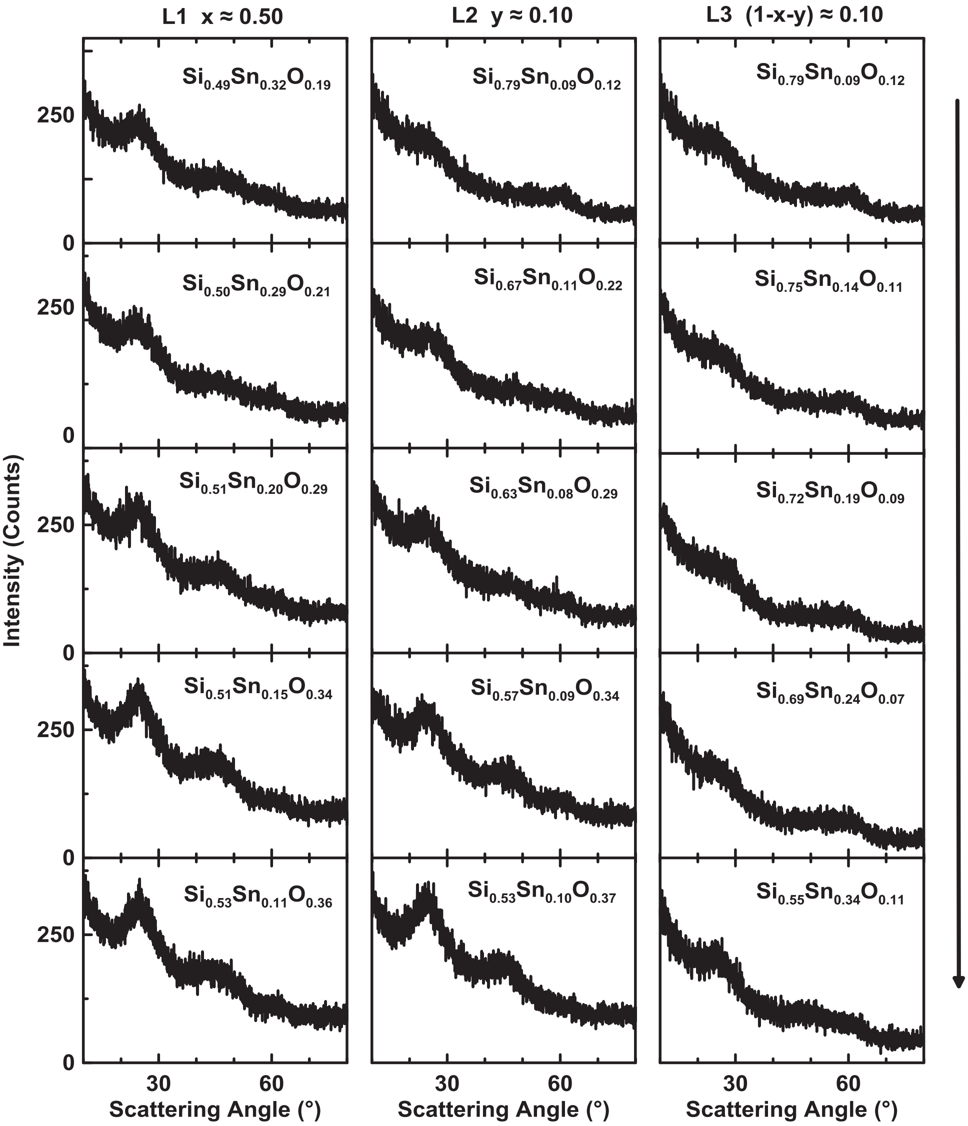

Figure 3. Selected XRD patterns of the $Si_xSn_yO_{1-x-y}$ films along composition lines L1, L2 and L3.

X-ray diffraction data were collected on a 5 × 5 grid that has the same positions as the 25 weigh disks used in coin cells. Figure 3 shows the selected XRD patterns of the $Si_xSn_yO_{1-x-y}$ films with $x \approx 0.50$, $y \approx 0.10$, and $(1-x-y) \approx 0.10$, respectively. The arrow in the figure indicates the same direction of composition variation in each column as that of the lines L1, L2, and L3 in Figure 2. The same convention is also used in the following figures. The vertical scales are the same for all of panels to more clearly show the minor phase variations. The films across the whole range represent a typical pattern of amorphous or nanostructured materials, as two broad peaks can be observed at about $2\theta = 25^\circ$ and 45° for all samples, with some variations in intensities.

Figures 4–7 show plots of potential vs. capacity for the coin cells made from the sputtered $Si_xSn_yO_{1-x-y}$ films over the first 1.5 cycles, as well as the differential capacity curves of the same electrodes. All plots are made on a per mole basis, so that changes in stoichiometry can be clearly discerned without being distorted by different atomic weights of the alloy constituents. Herein, w in $Li_w(Si_xSn_yO_{1-x-y})$ is defined as the moles of intercalated lithium per mole of $Si_xSn_yO_{1-x-y}$, as calculated based on the gravimetric capacity of the $Si_xSn_yO_{1-x-y}$ electrode. The voltage curves of all film electrodes have two sloping plateaus during the discharge-charge process. The appearance of these voltage curves is very similar to that for amorphous Si-Sn film electrodes, as previously reported.[7] Generally, the presence of sharp peaks in differential capacity curves are an indicator of the presence of 2-phase regions, usually caused by the formation of crystalline phases.[20,21] All of the differential curves are smooth and free from sharp peaks, which reflects the amorphous characteristics of the sputtered $Si_xSn_yO_{1-x-y}$ film electrodes. This is consistent with the XRD results.

For samples along line L1, as shown in Figure 4a, with increasing O content and decreasing Sn content from the top panel to the bottom panel, the reversible molar capacity (RMC) drops significantly but the irreversible molar capacity (IRMC) almost doesn't change. The shape of the differential capacity curves in Figure 4b is almost the same. However, the 0.5 V broad peak during charge is transformed to two broad peaks for the $Si_{0.49}Sn_{0.32}O_{0.19}$ sample shown in the top panel with a relatively high Sn content. Figure 5a shows voltage curves of the $Si_xSn_yO_{1-x-y}$ film at $y \approx 0.10$ (along line L2). With increasing O content and decreasing Si content, the observed trends of IRMC, RMC, and ICE resembles those of the $Si_xSn_yO_{1-x-y}$ electrodes at $x \approx 0.50$. In Figure 5b, the most notable variation in the differential capacity curves along composition line L2 occurs in the changes of the sharp cathodic peak between 0.4 V and 0.7 V. This peak disappears from the second cycle, which might be partly attributable to the solid electrolyte interface (SEI) formation and partly to the

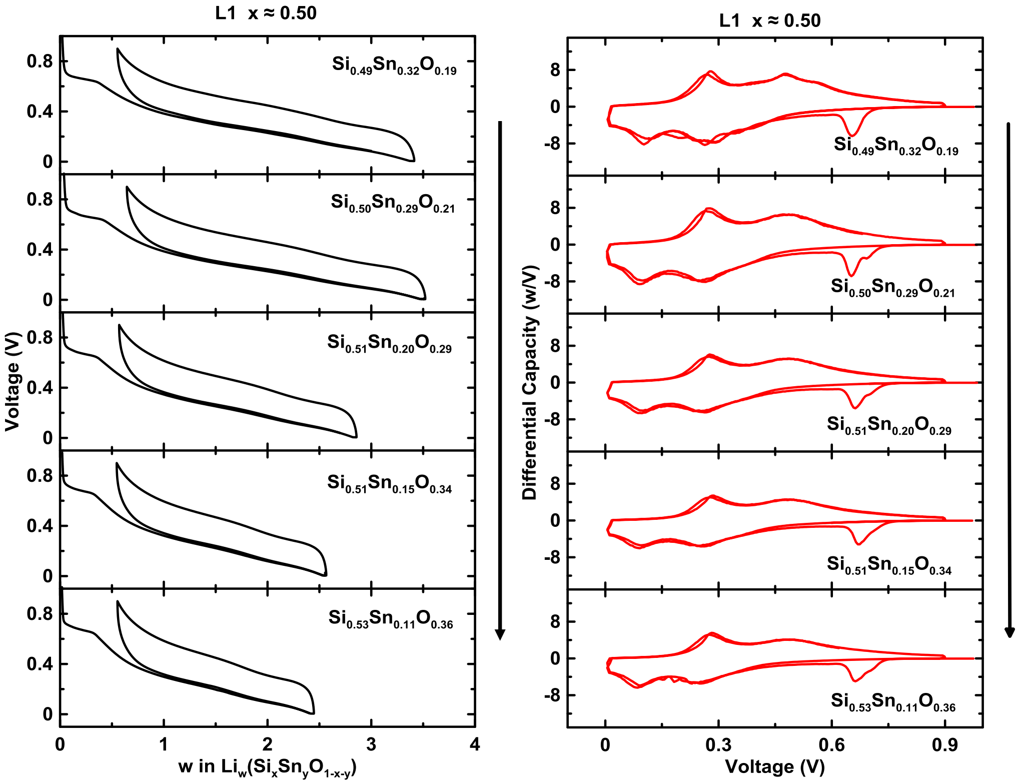

(a) (b)

Figure 4. (a) Voltage and (b) differential capacity curves of $Si_xSn_yO_{1\text{-}x\text{-}y}$ film electrodes along composition line L1.

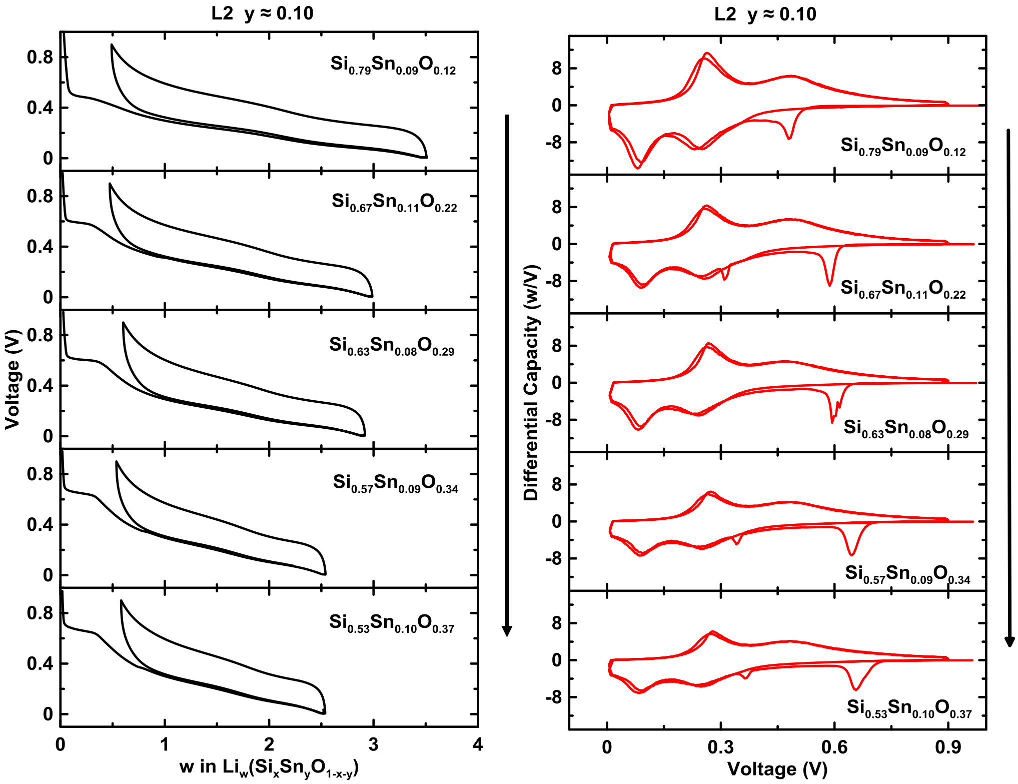

(a) (b)

Figure 5. (a) Voltage and (b) differential capacity curves of $Si_xSn_yO_{1\text{-}x\text{-}y}$ film electrodes along composition line L2.

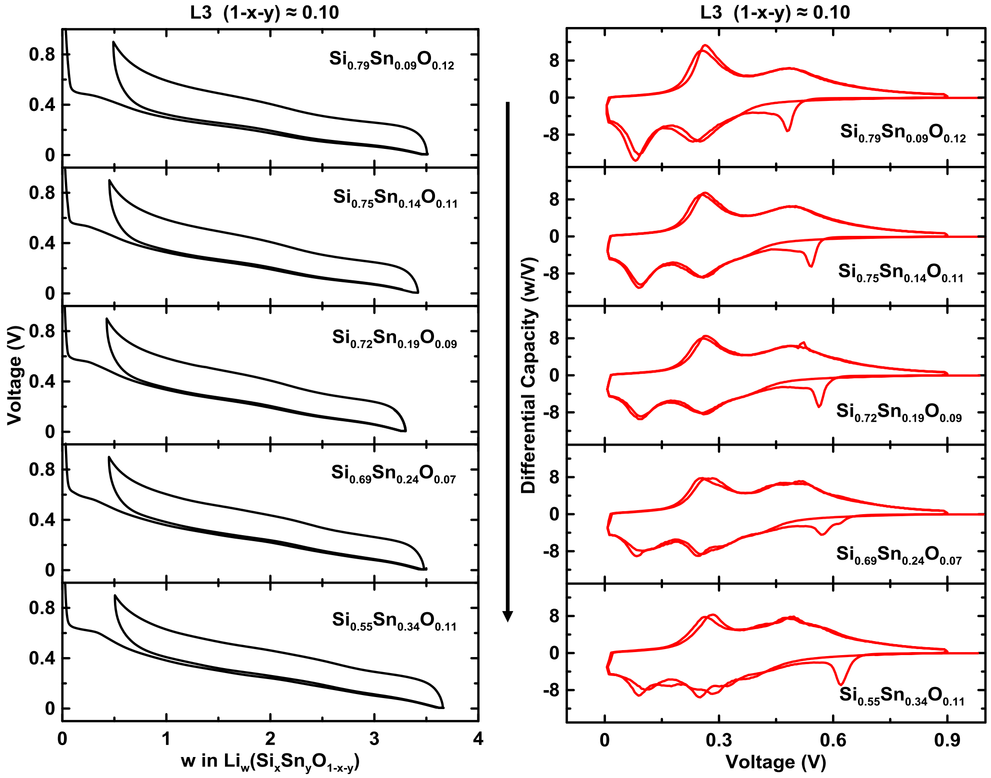

(a) (b)

Figure 6. (a) Voltage and (b) differential capacity curves of $Si_xSn_yO_{1\text{-}x\text{-}y}$ film electrodes along composition line L3.

irreversible reaction of oxygen with lithium, similar to that of Si-O films reported previously.[19,24] It can be observed that with increasing O content and decreasing Si content at $y \approx 0.10$, this peak shifts from 0.52 V to 0.72 V. This potential increase indicates that lithium insertion into $Si_xSn_yO_{1\text{-}x\text{-}y}$ electrodes during the first cycle might become more favorable.

Figure 6a shows the voltage curve of films with composition (1-x-y) ≈ 0.10 (along line L3). Along this line IRMC, RMC and ICE do not change significantly. A similar cathodic peak as seen along the L2 line also occurs in the differential capacity along the L3 line, as shown in Figure 6b. The peak increases in potential from 0.52 V to 0.67 V along L3. Apparently, the change in position of this peak mostly depends on only the Si content of the sputtered $Si_xSn_yO_{1\text{-}x\text{-}y}$ film. Lower Si content is favorable for first lithium insertion into the $Si_xSn_yO_{1\text{-}x\text{-}y}$ film.

Figure 7a shows a comparison of voltage curves for the most Si, Sn and O rich samples (P1, P2, and P3, respectively). IRMC, RMC and ICE are very similar for the most Si and Sn rich electrodes. By contrast, both RMC and ICE are lowest for the most O rich sample. Interestingly, the IRMC is similar for all the samples, indicating that it

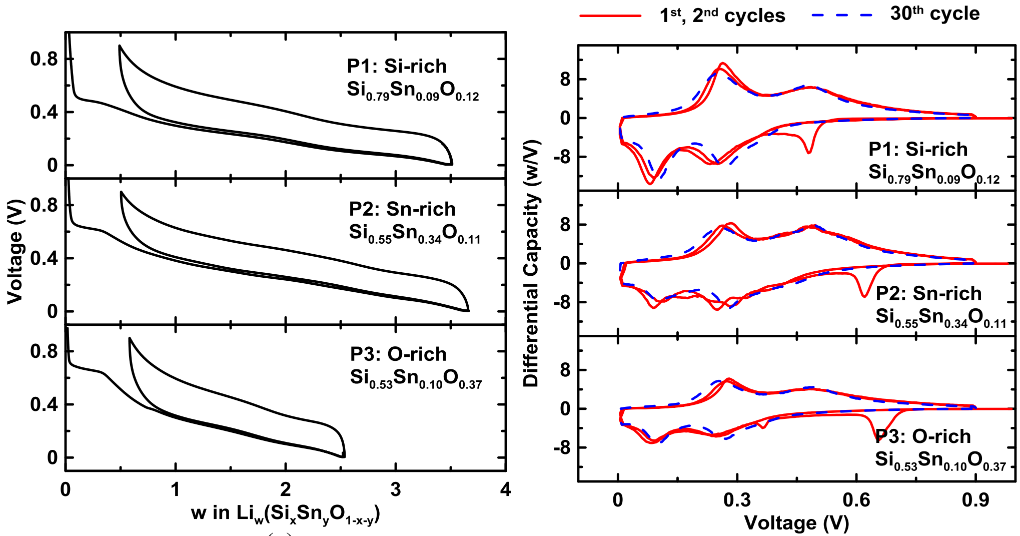

(a) (b)

Figure 7. (a) Voltage and (b) differential capacity curves of $Si_xSn_yO_{1\text{-}x\text{-}y}$ film electrodes at the most Si, Sn and O rich compositions (P1, P2, and P3, respectively).

Table I. The RMC, IRMC, and ICE of sputtered Si-Sn-O alloys.

Si (x)	Sn (y)	O (1-x-y)	RMC	IRMC	ICE (%)
0.79	0.09	0.12	3.0	0.49	86.0
0.72	0.06	0.22	2.4	0.50	83.2
0.63	0.08	0.29	2.3	0.60	79.4
0.60	0.05	0.35	1.9	0.57	77.2
0.54	0.09	0.37	2.1	0.67	75.6
0.75	0.14	0.11	3.0	0.45	86.8
0.67	0.11	0.22	2.5	0.47	84.2
0.57	0.17	0.26	2.7	0.65	80.5
0.57	0.09	0.34	2.0	0.54	78.9
0.53	0.10	0.37	2.0	0.58	77.1
0.72	0.19	0.09	2.9	0.43	87.1
0.65	0.17	0.18	2.6	0.52	83.4
0.53	0.25	0.22	2.9	0.69	80.6
0.55	0.13	0.32	2.1	0.54	79.5
0.53	0.11	0.36	1.9	0.55	77.4
0.69	0.24	0.07	3.0	0.45	87.1
0.58	0.27	0.15	2.9	0.54	84.4
0.50	0.29	0.21	2.9	0.64	81.7
0.51	0.20	0.29	2.3	0.57	80.1
0.51	0.15	0.34	2.0	0.55	78.7
0.62	0.34	0.04	3.4	0.45	88.5
0.55	0.34	0.12	3.2	0.51	86.2
0.49	0.32	0.19	2.9	0.55	83.8
0.47	0.29	0.24	2.6	0.57	82.3
0.45	0.25	0.30	2.4	0.58	80.1

is not greatly affected by the oxygen content. Therefore the lower ICE for the O-rich sample is simply the result of lower RMC. To examine if the amorphous state of sputtered $Si_xSn_yO_{1-x-y}$ film changes during cycling, differential capacity curves of the 30th cycle are compared with those of the 1st and 2nd cycles for the most Si, Sn and O rich samples in Figure 7b. Excepting the initial cathodic peak, the differential capacity peaks do not sharpen during cycling for the three samples. This suggests that the $Si_xSn_yO_{1-x-y}$ film electrodes over the range of compositions studied here can remain amorphous during the lithiation and delithiation process. This is characteristic of alloys having good cycling performance.[25] Regarding the cathodic peak between 0.4 V and 0.7 V, the position apparently depends on only Si content rather than Sn and O contents. This is consistent with the results along L1, L2, and L3 observed above.

Table I lists the RMC, IRMC, and ICE of 25 coin cells. To further understand the effects of Si, Sn, and O on electrochemical performance, contour plots of IRMC and RMC generated from all of the 25 coin cells data points as a function of composition are shown in Figures 8 and 9. Generally, the IRMC of $Si_xSn_yO_{1-x-y}$ thin film electrodes increases with increasing O content across the entire range of compositions up to an oxygen content of about 25%. Interestingly, the irreversible capacity does not increase for oxygen contents greater than this value. It may be that Si-oxide regions produced when the oxygen content is high become too large to react fully with Li. The trends in the RMC for $Si_xSn_yO_{1-x-y}$ electrodes can be observed in Figure 9. The RMC decreases with increasing O content and highest RMC occurs in the low O content region (alloys with the highest amount of active Si and Sn). The higher RMC occurs in the higher Sn content region. ICE of $Si_xSn_yO_{1-x-y}$ electrodes across the entire

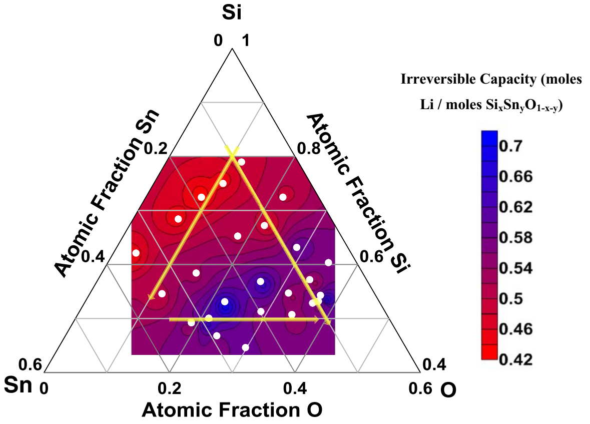

Figure 8. Contour map of the IRMC for $Si_xSn_yO_{1-x-y}$ film electrodes.

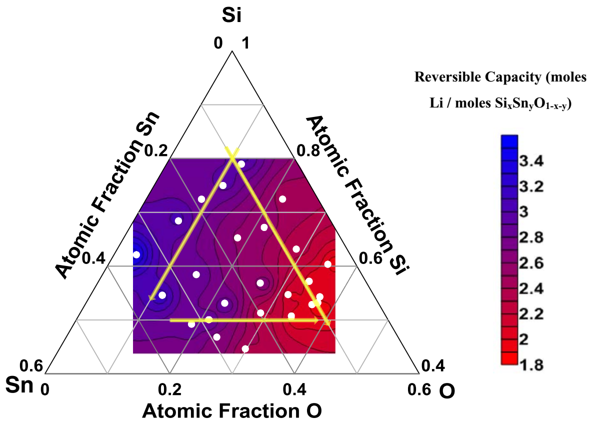

Figure 9. Contour map of RMC for $Si_xSn_yO_{1-x-y}$ film electrodes.

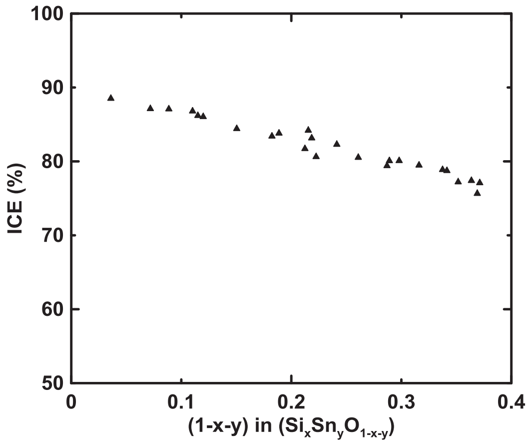

Figure 10. The ICE as a function of O content of $Si_xSn_yO_{1-x-y}$ film electrodes.

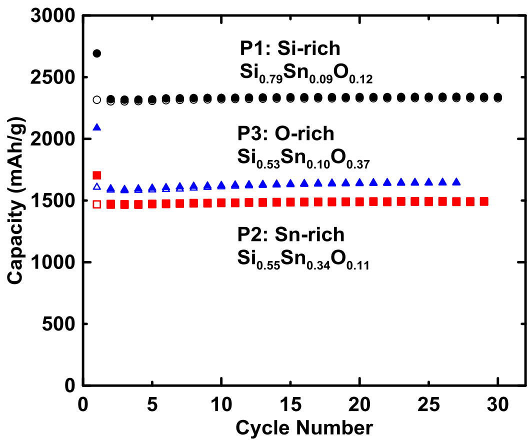

Figure 11. Cycling performance of the $Si_xSn_yO_{1-x-y}$ film at the most Si, Sn and O rich compositions (P1, P2, and P3, respectively).

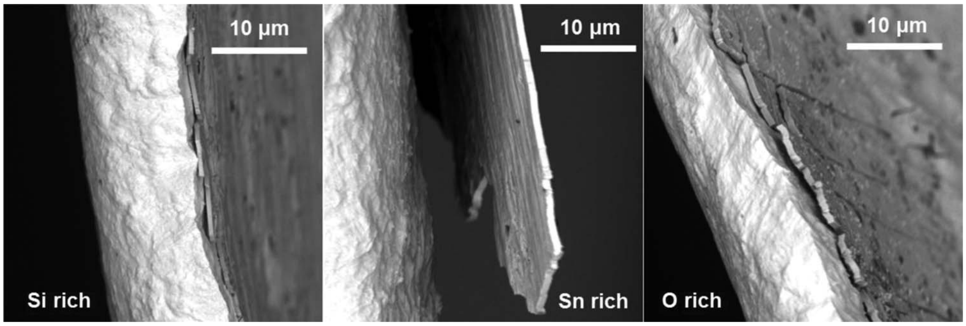

Figure 12. SEM images of the $Si_xSn_yO_{1-x-y}$ film at the most Si, Sn and O rich compositions (P1, P2, and P3, respectively).

sputtered composition range was also calculated based on IRMC and RMC values. A graph of ICE vs O content is shown in Figure 10. The ICE decreases significantly with increasing O content and an ICE of 88.5% can be observed at (1-x-y) $\approx$ 0.04. This indicates that some of the Li inserted in the film during the first lithiation becomes irreversibly trapped after reaction with oxygen.

All the sputtered $Si_xSn_yO_{1-x-y}$ film electrodes studied had good capacity retention. Figure 11 shows the gravimetric capacity versus cycle number for the electrodes at the most Si, Sn and O rich compositions samples. To calculate the volumetric capacities of these three samples the thickness of the sputtered films were accurately determined by tearing the electrodes and using scanning electron microscope (SEM) to observe the resulting cross-section. Figure 12 shows the SEM images of the most Si, Sn and O rich samples. All of the films are dense, with no apparent porosity. The thickness of the most Si rich film is about 0.5 μm, and the most Sn rich film has almost same thickness of about 0.75 μm as the most O rich film. The calculated densities based on the measured thickness are 3.35 g/cm^3, 4.20 g/cm^3, and 3.22 g/cm^3, respectively, for the most Si, Sn, and O rich samples. Using these density values and the observed capacity, the volumetric alloy capacity can be determined,[8] and were calculated to be about 2023 Ah/L and 1908 Ah/L for the Sn and O-rich samples (P2 and P3), respectively. The most Si rich sample (P1) has the highest volumetric capacity of about 2170 Ah/L. This is about 3 times that of the theoretical capacity of graphite (720 Ah/L).

Conclusions

$Si_xSn_yO_{1-x-y}$ samples with $0.45 < x < 0.80$, $0.05 < y < 0.35$, and $0.05 < (1-x-y) < 0.40$ were prepared by magnetron sputtering. XRD results of sputtered $Si_xSn_yO_{1-x-y}$ show that it is nanostructured or amorphous over the range of compositions studied here. As electrodes in Li cells, the sputtered films show excellent capacity retention across the entire composition range. This good cycling performance might be due to the homogenous expansion and contraction of the amorphous structure during cycling as indicated in the measured voltage and differential capacity curves. However, the presence of oxygen may help improve cycling by diluting volume change. In this sputtered Si-Sn-O system, on the other hand, O content has a significant effect on the IRMC, RMC and ICE: Generally, with increasing O content IRMC increases while RMC and ICE decrease gradually. IRMC doesn't change too much when O content is up to 25%. The higher RMC occurs in the higher Sn content region. The most Si rich sample shows the higher volumetric capacity compared to the most Sn and O rich samples. As well, low Si content can reduce difficulty of first lithium insertion into Si-Sn-O films. Further work should concentrate on improving ICE of high Si content samples with high volumetric capacity.

Acknowledgments

The authors acknowledge funding from NSERC and 3 M Canada, Co. under the auspices of the Industrial Research Chair and Discovery Grant programs and for financial support from the Dalhousie Research in Energy Advanced Materials and Sustainability (DREAMS) program.

References

1. M. N. Obrovac and V. L. Chevrier, *Chem. Rew.*, **114**, 11444 (2014).
2. B. A. Boukamp, G. C. Lesh, and R. A. Huggins, *J. Electrochem. Soc.*, **128**, 725 (1981).
3. M. N. Obrovac and L. Christensen, *Electrochem. Solid-State Lett.*, **7**, A93 (2004).
4. L. Y. Beaulieu, T. D. Hatchard, A. Bonakdarpour, M. D. Fleischauer, and J. R. Dahn, *J. Electrochem. Soc.*, **150**, A1457 (2003).
5. L. Y. Beaulieu, K. C. Hewitt, R. L. Turner, A. Bonakdarpour, A. A. Abdo, L. Christensen, K. W. Eberman, L. J. Krause, and J. R. Dahn, *J. Electrochem. Soc.*, **150**, A149 (2003).
6. L. Y. Beaulieu, K. W. Eberman, R. L. Turner, L. J. Krause, and J. R. Dahn, *Electrochem. Solid-State Lett.*, **4**, A137 (2001).
7. T. D. Hatchard and J. R. Dahn, *J. Electrochem. Soc.*, **151**, A1628 (2004).
8. M. N. Obrovac, L. Christensen, D. B. Le, and J. R. Dahn, *J. Electrochem. Soc.*, **154**, A849 (2007).
9. J. R. Dahn, S. Trussler, T. D. Hatchard, A. Bonakdarpour, K. C. Hewitt, and M. Fleischauer, *Chem. Mater.*, **14**, 3519 (2002).
10. H. J. Ahn, Y. S. Kim, K. W. Park, and T. Y. Seong, *Chem. Commun.*, **1**, 43 (2005).
11. M. Suzuki, J. Suzuki, K. Sekine, and T. Takamura, *J. Power Sources*, **146**, 452 (2005).
12. T. D. Hatchard, M. N. Obrovac, and J. R. Dahn, *J. Electrochem. Soc.*, **153**, A282 (2006).
13. A. Timmons and J. R. Dahn, *J. Electrochem. Soc.*, **153**, A1206 (2006).
14. M. A. Al-Maghrabi, J. S. Thorne, R. J. Sanderson, J. N. Byers, J. R. Dahn, and R. A. Dunlap, *J. Electrochem. Soc.*, **159**, A711 (2012).
15. J. R. Dahn, R. E. Mar, M. D. Fleischauer, and M. N. Obrovac, *J. Electrochem. Soc.*, **153**, A1211 (2006).
16. M. Miyachi, H. Yamamoto, H. Kawai, T. Ohta, and M. Shirakata, *J. Electrochem. Soc.*, **152** (10), A2089 (2005).
17. T. Kim, S. Park, and S. M. Oh, *J. Electrochem. Soc.*, **154** (12), A1112 (2007).
18. M. A. Al-Maghrabi, J. Suzuki, R. J. Sanderson, V. L. Chevrier, R. A. Dunlap, and J. R. Dahn, *J. Electrochem. Soc.*, **160**, A1587 (2013).
19. C. C. Nguyen, H. Choi, and S. W. Song, *J. Electrochem. Soc.*, **160**, A906 (2013).
20. I. A. Courtney and J. R. Dahn, *J. Electrochem. Soc.*, **144**, 2045 (1997).
21. I. A. Courtney, W. R. Mckinnon, and J. R. Dahn, *J. Electrochem. Soc.*, **146**, 59 (1999).
22. M V Reddy, G. V. S. Rao, and B. V. R. Chowdari, *Chem. Rew.*, **113**, 5364 (2013).
23. P. Liao, B. L. Macdonald, R. A. Dunlap, and J. R. Dahn, *Chem. Mater.*, **20**, 454 (2008).
24. Y. Yamada, Y. Iriyama, T. Abe, and Z. Ogumi, *J. Electrochem. Soc.*, **157**, A26 (2010).
25. V. L. Chevrier, L. Liu, D. B. Le, J. Lund, B. Molla, K. Reimer, L. J. Krause, L. D. Jensen, E. Figgemeier, and K. W. Eberman, *J. Electrochem. Soc.*, **161**, A783 (2014).